Iranian Journal of Astronomy and Astrophysics
Vol. 12, No. 3, Summer 2025, 249–266
©Available online at http://ijaa.du.ac.ir
DOI: 10.22128/ijaa.2026.3206.1242
Online ISSN: 2383–403X

**Iranian Journal of Astronomy and Astrophysics**

**Research Paper**

# The Relationship Between Recent and Old Star Formation in Dwarf Irregular Galaxies

Aysan Hemmatiortakand*[1] · Reza Rezaei[2] · Sina Mehdizadeh Fard[3]

[1] Department of Physics, Sharif University of Technology, Tehran, Iran;
*E-mail: aysanhemmatiortakand@gmail.com

[2] Department of Physics, Sharif University of Technology, Tehran, Iran;
E-mail: reza.rezaei@sharif.edu

[3] Department of Physics, Sharif University of Technology, Tehran, Iran;
E-mail: sinamfard1382@gmail.com

**Received:** 29 December 2025; **Accepted:** 9 January 2026; **Published:** 14 January 2026

**Abstract**. In this paper, we investigate the structural properties of local dwarf irregular galaxies, including optical scale lengths, position angles, and star formation rates, using data from the LITTLE THINGS survey. Our analysis is based on a sample of 24 dwarf irregular galaxies. Optical structural parameters are derived from $B$ and $V$ band images, while recent star formation rates are estimated using $H_\alpha$ data. Our goal is to identify correlations among properties associated with the same epoch, such as relationships between scale lengths measured in different optical bands, as well as to explore connections between different evolutionary stages. In particular, we examine how recent star formation relates to the $B-V$ color index, V-band luminosity and magnitude, and scale lengths as measured in optical wavelengths. We find that (A) there is a strong correlation between scale lengths measured in different optical bands and (B) Recent star formation rates show strong correlations with both galaxy magnitude and scale length in the visible filter, indicating that very recent star formation activity (on timescales of $\sim$1 Myr) is closely linked to older star formation activity (on timescales of $\sim$1 Gyr). The results for our sample are consistent and in good agreement with values reported in literature.

*Keywords*: Dwarf Irregular Galaxies, Star Formation Rate, LITTLE THINGS, Photometry, $H_\alpha$ Emission.

# 1 Introduction

Star formation in galaxies is commonly described using large-scale gravitational instability theory, where gas is expected to collapse and form stars once its density exceeds a critical threshold. While this theory successfully explains star formation in massive spiral galaxies, it is not able to predict how stars are formed in low-density systems, such as dwarf irregular galaxies, that do not reach the canonical critical value.

Dwarf irregular galaxies are low-mass, gas-rich systems that lack the structural characteristics of spiral or elliptical galaxies. Although individually faint, they constitute a significant fraction of the local galaxy population and can provide valuable information for

* *Corresponding author*

This is an open access article under the **CC BY** license.

studying star formation under conditions of low metallicity and low gas density. It is due to the importance of dwarf galaxies in understanding star formation at low gas densities that several surveys have compiled datasets of nearby dwarf systems, including the *LITTLE THINGS* sample, with the goal of characterizing their star-forming properties [1–3].

The star formation rate (SFR) measures the mass of gas a galaxy converts into stars per unit time, providing an overall picture of its ongoing growth. Star formation activity can be traced over a wide range of timescales using multiwavelength observations, as different tracers are sensitive to stellar populations of different ages. $H_\alpha$ emission is produced when ultraviolet radiation from young, massive O- and B-type stars ionizes the galaxy's interstellar gas. $H_\alpha$ emission traces the most recent star-forming activity on timescales of $\sim$10 Myr, whereas optical emission (e.g., UBV bands) reflects the integrated star formation history over Gyr timescales, and near-infrared (JHK) emission indicates the cumulative star formation throughout a galaxy's life [13]. For instance, Hunter et al. (2012) [1] derived SFRs from the combined luminosity of $H_\alpha$ and R-band images, while Leroy et al. (2012) [4] estimated SFRs using $H_\alpha$, UV, and infrared (IR) data.

In this work, we investigate the recent star formation activity of 24 nearby dwarf irregular galaxies using continuum-subtracted $H_\alpha$ imaging. The paper is organized as follows. In Sections 2 and 3, we present the observations and data reduction. The results are discussed in Section 4, followed by the Discussion and Summary in Sections 5 and 6, respectively.

## 2 Observations

The images of galaxies referenced in this paper were sourced from the (Local Irregulars That Trace Luminosity Extremes, The $H_I$ Nearby Galaxy Survey) database, a multi-wavelength dataset comprising 37 Dwarf Irregular and 4 Blue Compact Dwarf Galaxies.

We analyzed 24 Dwarf Irregular Galaxies from this sample using U, B, V, and $H_\alpha$ filters, with observations conducted at Lowell Observatory. Our sample can be categorized into four morphological subtypes within the irregular category: Magellanic irregular galaxies (Im), Barred Magellanic irregulars (IBm), Barred Magellanic irregulars with spiral features (IB(s)m), and Intermediate-barred Magellanic irregulars with spiral features (IAB(s)m).

Two types of $H_\alpha$ images were used in this study: one including the stellar continuum and one continuum-subtracted. The continuum-subtracted frame was obtained by subtracting an image captured through a continuum-only off-band filter (centered at 6440 Å with FWHM 95 Å) from the original $H_\alpha$ exposure. It should be noted that the continuum-subtracted image still contains [NII] emission, as these lines at 6548 Å and 6583 Å lie within the passband of the narrow-band $H_\alpha$ filter (FWHM $\approx$ 30 Å).

A complete table of the objects and images discussed in this study is provided in Appendix A.

## 3 Data Reduction

Photometric scale lengths are tools for quantifying galaxy size and structure. These characteristic radii are typically defined either at specific surface-brightness thresholds—such as the B-band isophotal radius $R^B_{25}$ [5,6] and the Holmberg radius $R^B_H$ [3,7,8]—or derived from parametric model fits to the surface-brightness profile, such as the exponential scale length $R^V_D$ [9,10] and the half-light radius $R^V_{1/2}$ [5].

We define $R^B_{25}$ as the semi-major axis of the ellipse fitted to the $\mu_B = 25$ mag arcsec$^{-2}$ isophote on the extinction–corrected B-band image, using $E(B-V)_f$ from Hunter and

Elmegreen 2004 [2]. Similarly, $R_H^B$ is defined as the semi-major axis of the ellipse fitted to the $\mu_B = 26.5 + 0.22 - 0.149(B-V)$ mag arcsec$^{-2}$ isophote, where $B-V$ is averaged over radii where the color is well defined [3,8]. In both cases, the uncertainty reflects the fitting error in the ellipse parameters derived from the respective isophotal contour.

For most disk-like galaxies, an exponential fit provides an adequate description of the outer surface-brightness profile, following de Vaucouleurs's two-component model of a $R^{1/4}$ bulge plus an exponential disk [5]. This paradigm was then tested and confirmed in the outer parts of spiral and S0 galaxies by Freeman [9], in dwarf ellipticals of the Fornax cluster by Caldwell & Bothun [11], and in low-surface-brightness dwarf irregulars of the Virgo cluster by Impey et al. [12]. By fitting an exponential function of the form

$$I(x) = \exp\left(-\frac{x - x_0}{R_D^V}\right), \tag{1}$$

where $x_0$ denotes the center of the light profile (see Figure 1), we determined $R_D^V$, with its uncertainty given by the $1\sigma$ width of the $R_D^V$ distribution from $n = 1000$ Gaussian-noise bootstrap realizations.

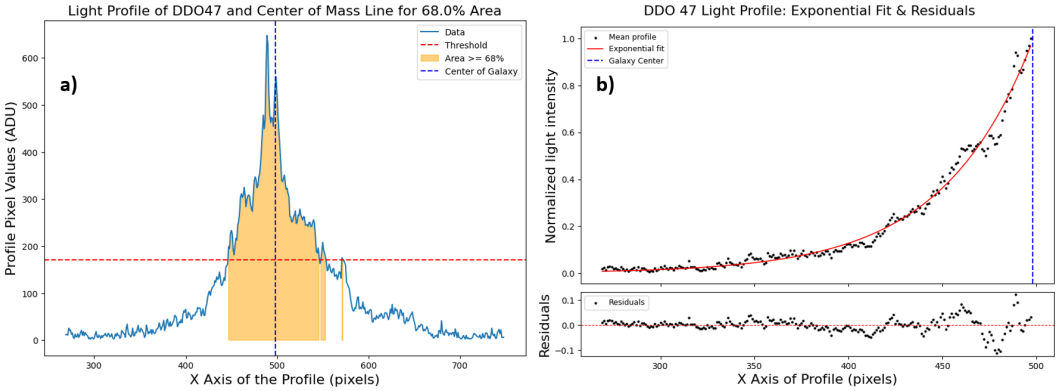


Figure 1: a) Light profile of DDO 47, plotted in ADU along the major axis. The shaded region contains 68% of the total integrated flux. The galaxy center is defined as the centroid of this region (dashed blue line), with the flux threshold used to define it shown in red. b) Normalized light profile of DDO 47 along the major axis, with exponential fit (red) and residuals. The galaxy center is marked by a dashed blue line.

To determine the half-light radius, we use the integrated intensity diagram of a galaxy based on a radial exponential intensity profile. The integral over pixels above a threshold $I_l$ is

$$L(I_l) = 2\pi I_0 R_D^2 \left[1 - \frac{I_l}{I_0} - \ln\left(\frac{I_l}{I_0}\right)\right], \tag{2}$$

where $I_0$ and $R_D$ are the central intensity and disk scale length. Assuming $\ln(I_l/I_0)$ is roughly constant at the galaxy edges yields

$$\frac{dL}{dI_l} \propto -\left[1 - \ln\left(\frac{I_l}{I_0}\right)\right], \tag{3}$$

implying a linear relation between $L$ and $I_l$.

Including a uniform background $I_b$ changes the derivative sharply,

$$\frac{dL}{dI_b} = \text{const} - \beta A\,\delta(I_l - I_b), \tag{4}$$

so for $I_l < I_b$, $L$ is the total image intensity, and as $I_l$ surpasses $I_b$, pixels above background define the galaxy contour. In practice, non-uniform noise broadens the spike in $dL/dI_l$ near $I_b$, complicating $L$ vs. $I_l$ and underestimating size. We use this behavior to identify the outermost contour.

In the linear regime we fit a line, extracting slope $a$, intercept $b$, and uncertainty $\sigma_b$. We find the intersection of $L(I_l)$ with

$$aI_l + b + n_{\text{err}}\,\sigma_b, \tag{5}$$

fit an ellipse to that contour, and plot its semi-major axis $R$ against $n_{\text{err}}$. The local minimum of $\frac{dR}{dn_{\text{err}}}$ marks a stable $R$ giving the full-light radius and intensity. We then locate the contour where intensity is half the full-light value, fit an ellipse without constraining the position angle, and define its semi-major axis as the half-light radius $R^V_{1/2}$. The final values for all scale lengths and position angles are reported in Table 1 (see Section 4).

The original $H_\alpha$ frames, containing both the continuum and background stars, were used to align the continuum-subtracted images with those taken in the visible filter, ensuring a uniform pixel scale and resolution across all wavelengths. In this study, we use equation 15 [2] to calculate the SFR from recent star-forming activity, based on the total luminosity of $H_\alpha$ ($L_{H\alpha}$) emission in continuum-subtracted images,

$$\text{SFR}\left(M_\odot\,\text{yr}^{-1}\right) = 5.96 \times 10^{-42}\; L_{H\alpha}\left(\text{erg}\,\text{s}^{-1}\right). \tag{6}$$

The $H_\alpha$ luminosity, $L_{H\alpha}$, is derived from the galaxy's emission flux at this wavelength, $F_{H\alpha}$. Due to the noisy nature of the continuum-subtracted images, we adopted a threshold whereby only pixels with values $\geq 4$ ADU contribute to $F_{H\alpha}$. Despite this cutoff, the images still exhibit a substantial amount of speckle noise. Since $F_{H\alpha}$ is computed as an integral over all thresholded pixels, residual speckle noise introduces systematic uncertainty into the final luminosity estimate.

To address this, we evaluated four de-noising techniques to identify the most effective method for our dataset: the Median filter [14], Lee filter [15], Kuan filter [16], and the Non-Local Means (NLM) filter [17] (Figure 2).

Among the four techniques evaluated, the Non-Local Means (NLM) filter proved to be the most effective across our dataset, successfully reducing speckle noise while relatively preserving the original flux values.

The NLM denoising method is a type of non-local noise reduction algorithm that operates based on similarities between different regions of an image within a given radius. The algorithm used in this method has three variable parameters: $p$, defines the box dimensions used for noise removal, $h$, controls the intensity of speckle noise reduction, and $d$, which represents the radius within which the algorithm searches for similar patches.

The parameters we used are:

$$h = 1.15\,\sigma, \quad p = 5, \quad d = 3,$$

where $\sigma$ is the image standard deviation.

The error due to the NLM method was estimated by bootstrapping different sets of parameters. The galaxies' total flux in the $H_\alpha$ wavelength was then obtained by integrating

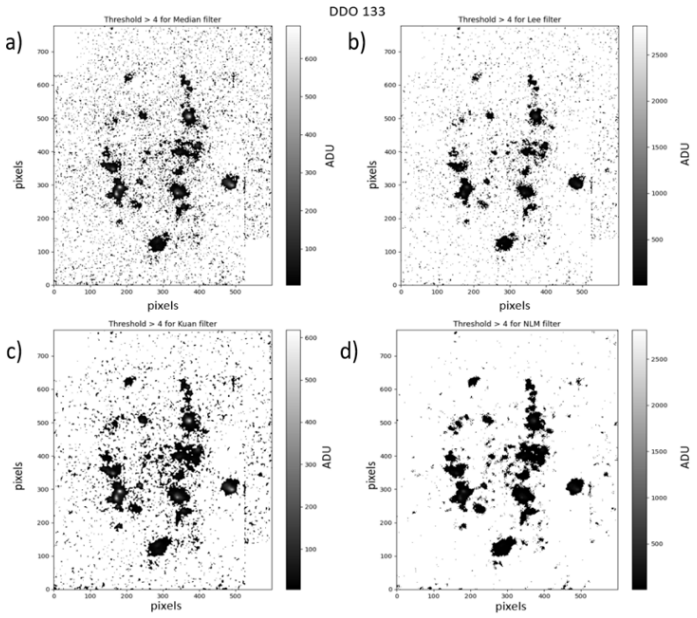


Figure 2: Results of applying four de-noising techniques to a continuum-subtracted image of DDO 133: a) Median filter, b) Lee filter, c) Kuan filter, and d) Non-Local Means (NLM) filter.

over all the pixels in their respective images after de-noising. The integration error was determined using the resampling with replacement method [18].

We corrected for internal reddening due to gas ($E(B{-}V)_g = 0.1$) and foreground reddening ($E(B{-}V)_f$), adopting values reported by Hunter and Elmegreen (2004) [2]. Both corrections were applied using the reddening law formulated by Cardelli, Clayton, and Mathis (1989) [19]. In this method, the wavelength-dependent extinction coefficient $A_\lambda$ is computed using equation (7)

$$\left\langle \frac{A(\lambda)}{A(V)} \right\rangle = a(x) + \frac{b(x)}{R_V}, \tag{7}$$

where $x = 1/\lambda$ (in $\mu\mathrm{m}^{-1}$) and $R_V = 3.1$, suitable for diffuse interstellar medium such as dwarf galaxies.

For the $H\alpha$ emission line ($\lambda = 6563\,\text{Å}$), this corresponds to $x = 1.524\,\mu\mathrm{m}^{-1}$. The coefficients $a(x)$ and $b(x)$ are:

$$\begin{aligned} a(x) &= 1 + 0.17699y - 0.50477y^2 - 0.024247y^3 \\ &\quad + 0.72089y^4 + 0.01979y^5 - 0.77530y^6 + 0.32999y^7, \end{aligned} \tag{8}$$

$$\begin{aligned} b(x) &= 1.14336y - 2.23836y^2 + 1.07233y^3 \\ &\quad - 5.3834y^4 - 0.52215y^5 + 5.30260y^6 - 2.00909y^7, \end{aligned} \tag{9}$$

where y is defined as, $y = x - 1.82$.

To correct the observed flux $F_{\text{obs}}$ for extinction, we applied the standard relation:

$$F_{\text{corr}} = F_{\text{obs}} \times 10^{0.4A(\lambda)}, \tag{10}$$

To compute the total galaxy luminosity ($L_{H\alpha}$), we first used the reported distances to each galaxy (see Table 1) along with the corresponding integrated exposure times (listed in Table 3) to obtain instrumental luminosities. These were then calibrated into physical units using star formation rate (SFR) values reported by Hunter and Elmegreen (2004) [2], from which we derived a calibration coefficient specific to each instrument used to capture the images in this study. Star formation rates were then calculated using equation 15 and reported in Table 2.

# 4 Results

The structural and photometric parameters derived in Section 3 are summarized in Table 1 which lists distances, foreground reddening, half-light and full-light position angles and scale-lengths in V and B filters for each galaxy.

Table 1: Scale-lengths and related parameters for our galaxy sample.

| Object Name | $D$ (Mpc) [a] | $E(B-V)_f$ [b] | PA1 (°) [c] | PA2 (°) [d] | $R^V_{1/2}$ (kpc) [e] | $R^B_{25}$ (kpc) [f] | $R^B_H$ (kpc) [g] | $R^V_D$ (kpc) [h] |
|---|---|---|---|---|---|---|---|---|
| DDO 43 | 5.5 | 0.05 | 155.6 | 170.9 | $0.866 \pm 0.026$ | $0.947 \pm 0.009$ | $1.382 \pm 0.005$ | $0.372 \pm 0.002$ |
| DDO 46 | 5.5 | 0.05 | 158.6 | 140.4 | $0.990 \pm 0.130$ | $0.961 \pm 0.006$ | $1.657 \pm 0.009$ | $0.704 \pm 0.029$ |
| DDO 47 | 5.2 | 0.02 | 78 | 78.7 | $2.300 \pm 0.428$ | $1.966 \pm 0.011$ | $4.109 \pm 0.026$ | $1.389 \pm 0.025$ |
| DDO 50 | 3.4 | 0.02 | 142.0 | 161.1 | $1.884 \pm 0.028$ | $3.056 \pm 0.015$ | $3.845 \pm 0.015$ | $0.870 \pm 0.031$ |
| DDO 52 | 6.0 | 0.03 | 1.3 | -4.3 | $0.368 \pm 0.038$ | $0.696 \pm 0.005$ | $2.029 \pm 0.010$ | $0.689 \pm 0.011$ |
| DDO 63 | 3.8 | 0.01 | 0.8 | 30.7 | $1.640 \pm 0.071$ | $1.534 \pm 0.040$ | $2.409 \pm 0.009$ | $1.427 \pm 0.150$ |
| DDO 69 | 0.8 | 0.00 | 77.8 | 70.3 | $2.891 \pm 0.015$ | $0.339 \pm 0.002$ | $0.562 \pm 0.002$ | $0.229 \pm 0.025$ |
| DDO 87 | 6.7 | 0.00 | 102.8 | 208.9 | $0.237 \pm 0.147$ | $1.473 \pm 0.074$ | $1.970 \pm 0.004$ | $1.131 \pm 0.061$ |
| DDO 101 | 9.0 | 0.01 | 82.6 | 69.1 | $1.653 \pm 0.037$ | $1.956 \pm 0.011$ | $2.930 \pm 0.006$ | $1.146 \pm 0.039$ |
| DDO 126 | 4.9 | 0.00 | 19.4 | 40.1 | $1.056 \pm 0.202$ | $1.404 \pm 0.007$ | $2.745 \pm 0.010$ | $0.513 \pm 0.019$ |
| DDO 133 | 6.1 | 0.00 | 0.8 | 1.7 | $2.720 \pm 0.058$ | $2.960 \pm 0.003$ | $4.147 \pm 0.008$ | $1.998 \pm 0.099$ |
| DDO 154 | 4.3 | 0.01 | 149.7 | 144.4 | $0.832 \pm 0.065$ | $1.094 \pm 0.010$ | $1.785 \pm 0.009$ | $0.585 \pm 0.125$ |
| DDO 155 | 2.2 | 0.01 | 126.3 | 51.0 | $0.333 \pm 0.012$ | N/A | $0.416 \pm 0.002$ | $0.154 \pm 0.003$ |
| DDO 165 | 4.8 | 0.01 | 175.4 | 181.1 | $1.651 \pm 0.063$ | $2.237 \pm 0.008$ | $3.274 \pm 0.007$ | $1.515 \pm 0.027$ |
| DDO 167 | 4.2 | 0.00 | 18.6 | 20.2 | $0.532 \pm 0.034$ | N/A | $0.584 \pm 0.002$ | $0.405 \pm 0.007$ |
| DDO 168 | 3.5 | 0.00 | 30.1 | 28.7 | $1.135 \pm 0.029$ | $1.793 \pm 0.008$ | $2.643 \pm 0.005$ | $0.769 \pm 0.015$ |
| DDO 187 | 2.5 | 0.00 | 144.9 | 157.1 | $0.445 \pm 0.016$ | N/A | $0.342 \pm 0.004$ | $0.287 \pm 0.014$ |
| NGC 1156 | 7.8 | 0.17 | 148.9 | 136.8 | $2.966 \pm 0.088$ | $2.961 \pm 0.015$ | $3.803 \pm 0.012$ | $0.919 \pm 0.103$ |
| NGC 1569 | 2.5 | 0.51 | 62.7 | 116.2 | $0.548 \pm 0.009$ | $0.628 \pm 0.002$ | $2.186 \pm 0.006$ | $0.191 \pm 0.012$ |
| NGC 2366 | 3.2 | 0.04 | 148.5 | 144.3 | $1.946 \pm 0.038$ | $2.477 \pm 0.014$ | $4.257 \pm 0.025$ | $1.395 \pm 0.002$ |
| NGC 4163 | 2.8 | 0.00 | 173.6 | 166.6 | $0.693 \pm 0.010$ | $0.772 \pm 0.001$ | $1.215 \pm 0.002$ | $0.244 \pm 0.001$ |
| NGC 4214 | 2.9 | 0.00 | 40.9 | 49.2 | $1.205 \pm 0.001$ | $2.194 \pm 0.004$ | $3.617 \pm 0.019$ | $0.310 \pm 0.004$ |
| UGC 8508 | 2.6 | 0.00 | 23.8 | 29.0 | $0.424 \pm 0.010$ | $0.690 \pm 0.001$ | $1.014 \pm 0.001$ | $0.286 \pm 0.005$ |
| WLM | 1.0 | 0.02 | 175.2 | 181.5 | $0.872 \pm 0.023$ | $1.171 \pm 0.004$ | $1.755 \pm 0.003$ | $0.749 \pm 0.024$ |

[a] Distance to the object [2].
[b] Foreground reddening [2].
[c] Position Angle of the ellipse fitted to the half-light contour.
[d] Position Angle of the ellipse fitted to the full-light contour.
[e] $R^V_{1/2}$ is the half-light radius in the V band.
[f] $R^B_{25}$ is the radius at the 25 mag arcsec$^{-2}$ surface-brightness level in the reddening corrected B band.
[g] $R^B_H$ is the Holmberg radius based on the reddening corrected B band.
[h] $R^V_D$ is the exponential disk scale length in the V band.
[i] Not available. This galaxy's surface-brightness did not reach 25 mag arcsec$^{-2}$.

In Figure 3, we show the correlation between each pair of the scale lengths discussed in section 3. The strongest linear correlation is between $R^B_{25}$ and $R^B_H$, where the Pearson coefficient is 0.91. This is expected, given that both quantities are derived from surface brightness measurements in the blue filter.

The strongest monotonic correlation is between $R^B_{25}$ and $R^V_{1/2}$. Despite originating from different filters, both are sensitive to the size of the inner regions of the galaxy during a similar era.

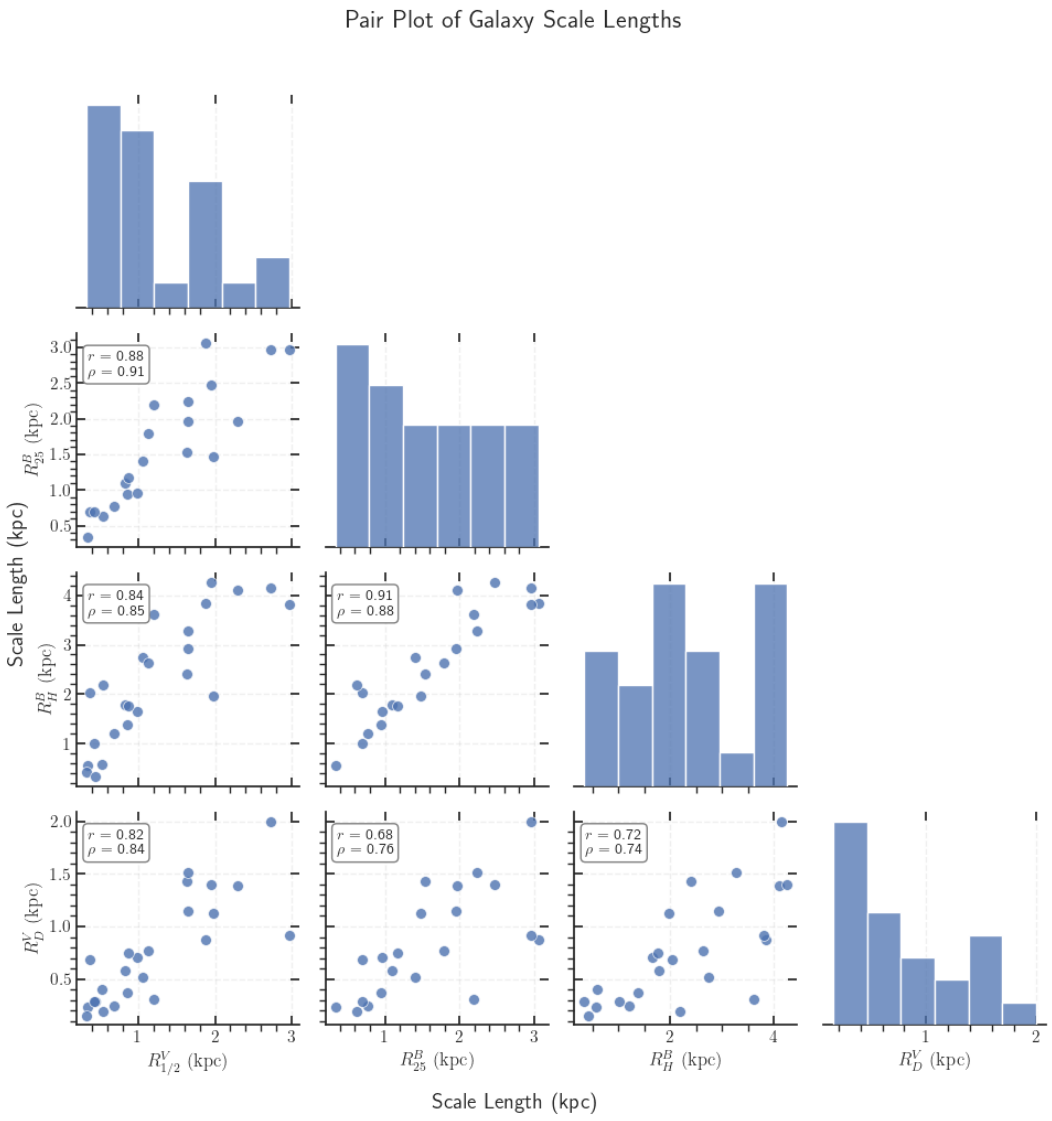


Figure 3: Cross-comparison of scale lengths $R^V_{1/2}$, $R^B_{25}$, $R^B_H$, and $R^V_D$ (in kpc), analyzed using Pearson ($r$) and Spearman ($\rho$) correlation coefficients.

Both the half-light radius $R^V_{1/2}$ and the exponential scale length $R^V_D$ are based on the assumption that dwarf galaxies exhibit an approximately exponential radial brightness profile. This theoretical similarity underlies the substantial correlation between these two parameters, where $r = 0.82$ and $\rho = 0.84$. Here, $r$ is the Pearson correlation coefficient, which measures linear correlation, and $\rho$ is the Spearman rank correlation coefficient, which captures monotonic relationships regardless of linearity.

Our model of a simple isotropic exponential profile suggests a constant ratio between the half-light radius and the exponential scale length. $R^V_{1/2}$ for our galaxy disk model can be calculated using the equations below, and equation 13 denotes the theoretical relationship

between the two values

$$L = \int_0^{\infty} 2\pi r\, I(r)\, dr = \int_0^{\infty} 2\pi r\, I_0 \exp\left(-\frac{r}{R_D^V}\right) dr = 2\pi I_0 \left(R_D^V\right)^2, \tag{11}$$

$$\begin{aligned}\frac{L}{2} = \pi I_0 \left(R_D^V\right)^2 &= \int_0^{R_{1/2}^V} 2\pi r\, I_0 \exp\left(-\frac{r}{R_D^V}\right) dr \\ &= 2\pi I_0 \left(R_D^V\right)^2 \left[1 - \exp\left(-\frac{R_{1/2}^V}{R_D^V}\right)\left(1 + \frac{R_{1/2}^V}{R_D^V}\right)\right],\end{aligned} \tag{12}$$

$$\exp\left(-\frac{R_{1/2}^V}{R_D^V}\right)\left(1 + \frac{R_{1/2}^V}{R_D^V}\right) = \frac{1}{2} \quad \Rightarrow \quad \frac{R_{1/2}^V}{R_D^V} \approx 1.68. \tag{13}$$

Figure 4 shows the histogram of the ratio $R_{1/2}^V/R_D^V$ for our galaxy sample. The theoretical value derived in Equation 13 is indicated by the red dashed line. Using the scale-length measurements reported in Table 1, we find a mean ratio of 1.802 with a standard deviation of 0.752. Overall, this agreement supports the validity of the exponential disk model, which provides a simple yet effective description of the galaxy intensity profile, successfully reproducing both the integrated intensity curve and the relationship between the exponential disk scale length, $R_D^V$, and the half-light radius, $R_{1/2}^V$.

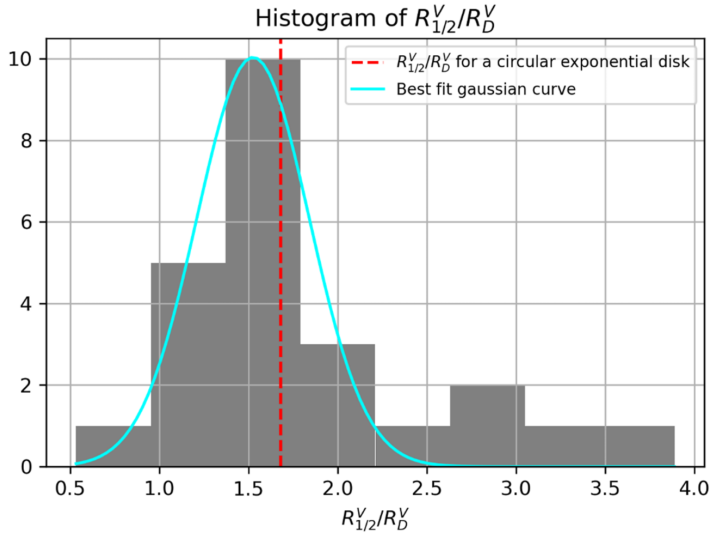


Figure 4: Histogram of the ratio $R_{1/2}^V/R_D^V$ for the galaxy sample. The red dotted line indicates the theoretical value expected for an exponential disk, while the cyan curve shows a Gaussian fit to the distribution.

Table 2 summarizes the star formation and atomic mass gas for our galaxy sample. It lists for each object the logarithm of the star formation rate $\log_{10}$SFR $\pm$ Error ($M_\odot\,\mathrm{yr}^{-1}$) and the logarithm of the total galactic atomic gas mass (Mass/$M_\odot$) [2].

Figure 5 presents the correlation between the logarithm of recent star formation rates (SFR; $\approx$ 1 Myr) and four key galaxy properties: atomic gas mass (panel (a)), half-light

Table 2: Star formation and atomic gass mass for our galaxy sample.

| Object Name | $\log_{10}$SFR $\pm$ Error ($M_\odot\,\mathrm{yr}^{-1}$) | $\log_{10}(\mathrm{Mass}/M_\odot)$ [a] |
|---|---|---|
| DDO 43 | $-2.3042 \pm 0.1410$ | 8.10 |
| DDO 46 | $-2.4526 \pm 0.1407$ | 8.26 |
| DDO 47 | $-1.8070 \pm 0.1179$ | 8.73 |
| DDO 50 | $-1.4680 \pm 0.1632$ | 8.99 |
| DDO 52 | $-3.0816 \pm 0.1324$ | 8.10 |
| DDO 63 | $-3.8183 \pm 0.1773$ | 8.31 |
| DDO 69 | $-3.8183 \pm 0.1565$ | 7.13 |
| DDO 87 | $-2.0934 \pm 0.0655$ | 8.37 |
| DDO 101 | $-2.4146 \pm 0.1213$ | 7.40 |
| DDO 126 | $-2.3666 \pm 0.1417$ | 8.27 |
| DDO 133 | $-1.8812 \pm 0.1521$ | 8.71 |
| DDO 154 | $-2.4684 \pm 0.1444$ | 8.62 |
| DDO 155 | $-2.7664 \pm 0.1556$ | 7.13 |
| DDO 165 | $-2.3876 \pm 0.1401$ | 8.32 |
| DDO 167 | $-2.8590 \pm 0.1419$ | 7.39 |
| DDO 168 | $-2.2641 \pm 0.1611$ | 8.48 |
| DDO 187 | $-3.5539 \pm 0.1383$ | 7.48 |
| NGC 1156 | $-0.6408 \pm 0.1706$ | 9.16 |
| NGC 1569 | $-0.4364 \pm 0.1757$ | 8.12 |
| NGC 2366 | $-1.1036 \pm 0.1704$ | 8.96 |
| NGC 4163 | $-2.9662 \pm 0.1631$ | 7.31 |
| NGC 4214 | $-0.8564 \pm 0.0476$ | 8.88 |
| UGC 8508 | $-2.8380 \pm 0.1315$ | 7.54 |
| WLM | $-2.6982 \pm 0.1600$ | 7.90 |

[a] Total galactic atomic gas mass. The H I mass has been multiplied by 1.34 to account for He [2].

radius in the V-band ($R^V_{1/2}$; panel (b)), apparent magnitude in the V-band (panel (c)), and the (B - V) color index (panel (d)). Each data point is shaped according to galaxy morphology, and color-coded by a third parameter, either the exponential disk scale length $R^V_D$ or atomic gas mass.

In panel (a), recent star formation shows a strong positive correlation with atomic gas mass. This trend supports the expectation that galaxies with larger reservoirs of neutral hydrogen and helium are more capable of sustaining ongoing star formation. The color gradient, mapped to $R^V_D$, provides an additional sense of galaxy size and spatial extent.

Panels (b) and (c) examine how recent star formation activity relates to photometric properties in the V-band, which primarily trace older stellar populations ($\sim$1 Gyr). Panel (b) shows a moderate trend between star formation rate and half-light radius ($R^V_{1/2}$), suggesting that spatial extent may play a limited role in sustaining star formation. Panel (c), however, shows a clear and strong correlation between recent star formation rate and absolute V-band magnitude ($M_V$), with Spearman and Pearson coefficients of $\rho = -0.89$ and $r = -0.95$. The $M_v$ values have been corrected for dust extinction using $A_V = 3.1 \times E(B-V)$. This result indicates that galaxies with brighter intrinsic optical luminosity tend to have higher current star formation rates.

In panel (d), the distribution exhibits a weak negative correlation between (B - V) color index and recent SFR. Redder galaxies (higher (B - V)) show systematically lower star formation rates, while bluer galaxies span a wide range of SFR values. This asymmetry

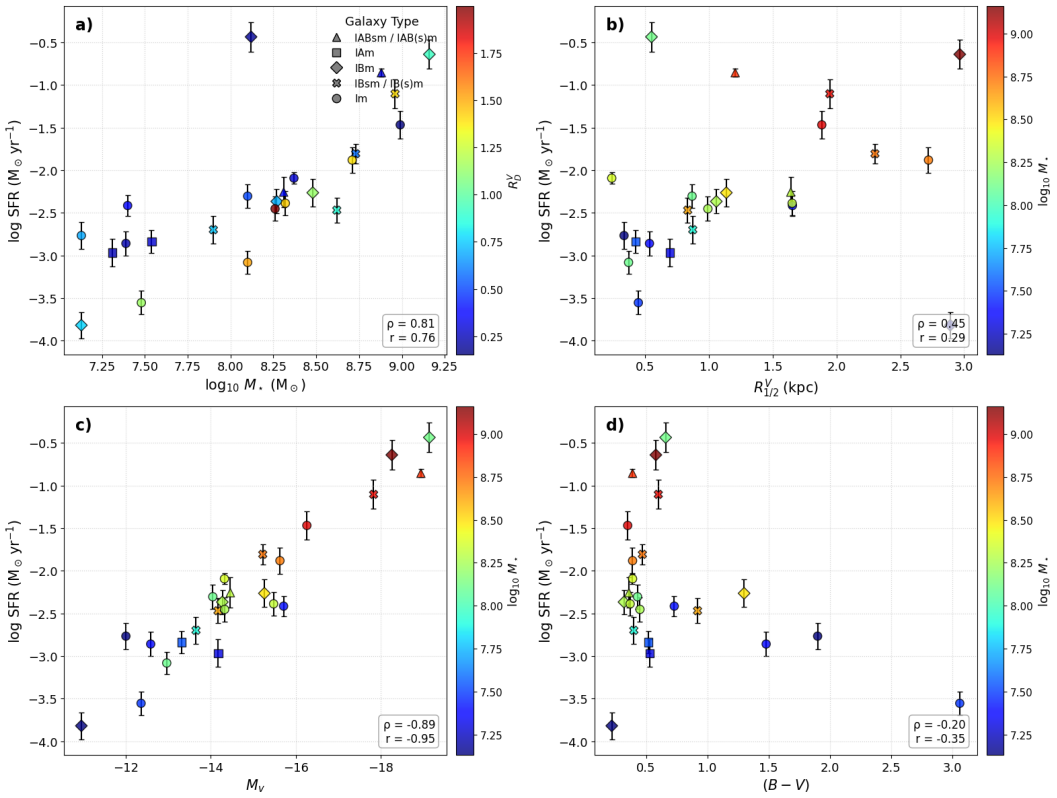


Figure 5: Comparisons between the logarithm of the star formation rate (SFR, in $M_\odot\,\mathrm{yr}^{-1}$) and key galaxy properties. Each panel shows individual galaxies with error bars and encodes two additional parameters: color and marker shape. (a) $\log(\mathrm{SFR}/M_\odot\,\mathrm{yr}^{-1})$ vs. $\log(M_*/M_\odot)$, colored by $R_D^V$ (kpc). (b) $\log(\mathrm{SFR}/M_\odot\,\mathrm{yr}^{-1})$ vs. $R_{1/2}^V$ (kpc), colored by $\log(M_*/M_\odot)$. (c) $\log(\mathrm{SFR}/M_\odot\,\mathrm{yr}^{-1})$ vs. V-band absolute magnitude $M_V$, colored by $M_*/M_\odot$. (d) $\log(\mathrm{SFR}/M_\odot\,\mathrm{yr}^{-1})$ vs. $B-V$, colored by $\log(M_*/M_\odot)$. In each panel, the Spearman rank correlation coefficient ($\rho$) and Pearson correlation coefficient ($r$) are annotated in the lower-right corner.

implies that although blue color is a necessary condition for high SFR, it is not sufficient and the sparsely populated region at high (B - V) and high SFR further supports this interpretation. We acknowledge that this pattern may be influenced by the limited size of our sample, and plan to expand the dataset in future work to test the validity of this claim. It is worth noting that B-V color gradient map hints at different star formation epochs for each galaxy.

Furthermore, we examined the correlation between galaxy size and stellar mass. Figure 6 provides a visual representation of these relationships. Panel (a) shows the half-light radius, $R_H^B$, as a function of galaxy mass, $\log_{10}(M_\star/M_\odot)$, while Panel (b) explores the corresponding relation between $R_{25}^B$ and galaxy mass. In both panels, we find a positive correlation between galaxy radius and stellar mass, as quantified by both Pearson and Spearman correlation coefficients. The solid lines indicate linear least-squares fits to the data, highlighting the overall trend of increasing galaxy size with increasing stellar mass.

The same strong correlation can not be found for $R_{1/2}^V$ and $R_D^V$ since they are dependent

on many more factors other than just the total luminosity of the galaxy such as galaxy concentration in the center and density profile.

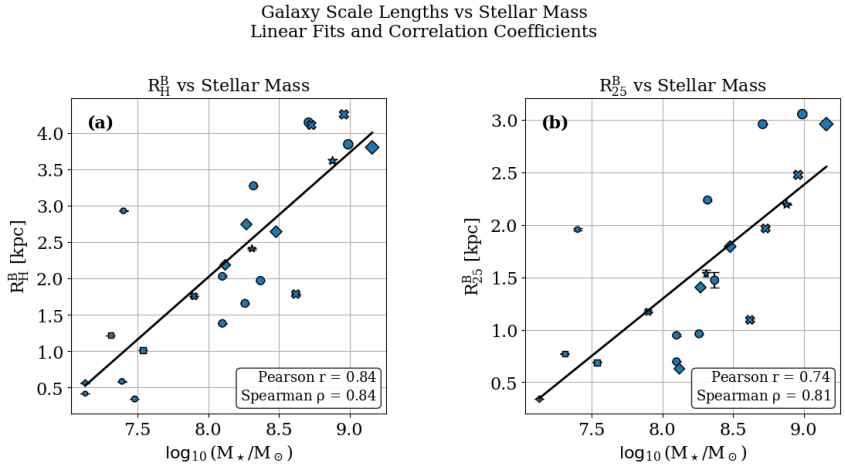


Figure 6: Correlation between galaxy size and stellar mass. Panel (a) shows the relation between the half-light radius $R_H^B$ and galaxy mass, $\log_{10}(M_\star/M_\odot)$, while Panel (b) presents the corresponding relation for $R_{25}^B$. In both panels, a positive correlation is observed, quantified using Pearson and Spearman correlation coefficients, with solid lines indicating linear least-squares fits.

# 5 Discussion

We compared our galaxy scale lengths (Table 1) with the corresponding values reported by Hunter and Elmegreen (2006) [3]. A visual representation of these comparisons is shown in Figure 7 as scatter plots. Panel (a) presents our measurements of the half-light radius against the reported values, Panels (b), (c), and (d) show comparisons for $R_{25}^B$, $R_H^B$, and the exponential radius to their respective, published values. The symbol sizes and shapes were chosen to represent the galaxy mass and type of each object. In all cases, our results demonstrate good consistency with those of Hunter and Elmegreen, indicating that our methodology is in agreement with established literature. In addition, we were able to determine values not reported in the original paper: $R_{25}^B$ for DDO 87 and NGC 1569, and $R_H^B$ for DDO 46 and NGC 1569.

The $H_\alpha$ star formation rate (SFR) calibration has evolved over the years in response to stellar population models, IMF assumptions, and the study of different galaxy types. The relation between $L_{H_\alpha}$ and recent star formation rate was introduced by Kennicutt in 1998 [20] for galaxies with continuous star formation, a Salpeter IMF [23], and typical spiral metallicities

$$\text{SFR}\ (M_\odot\,\text{yr}^{-1}) = 7.9 \times 10^{-42}\ L_{H_\alpha}\ (\text{erg}\,\text{s}^{-1}). \tag{14}$$

Recognizing that dwarf irregular galaxies are metal-poor, have low dust content, and often very low SFRs, Hunter and Elmegreen [2] adapted Kennicutt's relation to these systems, lowering the coefficient to

$$\text{SFR}\ \left(M_\odot\,\text{yr}^{-1}\right) = 5.96 \times 10^{-42}\ L_{H\alpha}\ \left(\text{erg}\,\text{s}^{-1}\right). \tag{15}$$

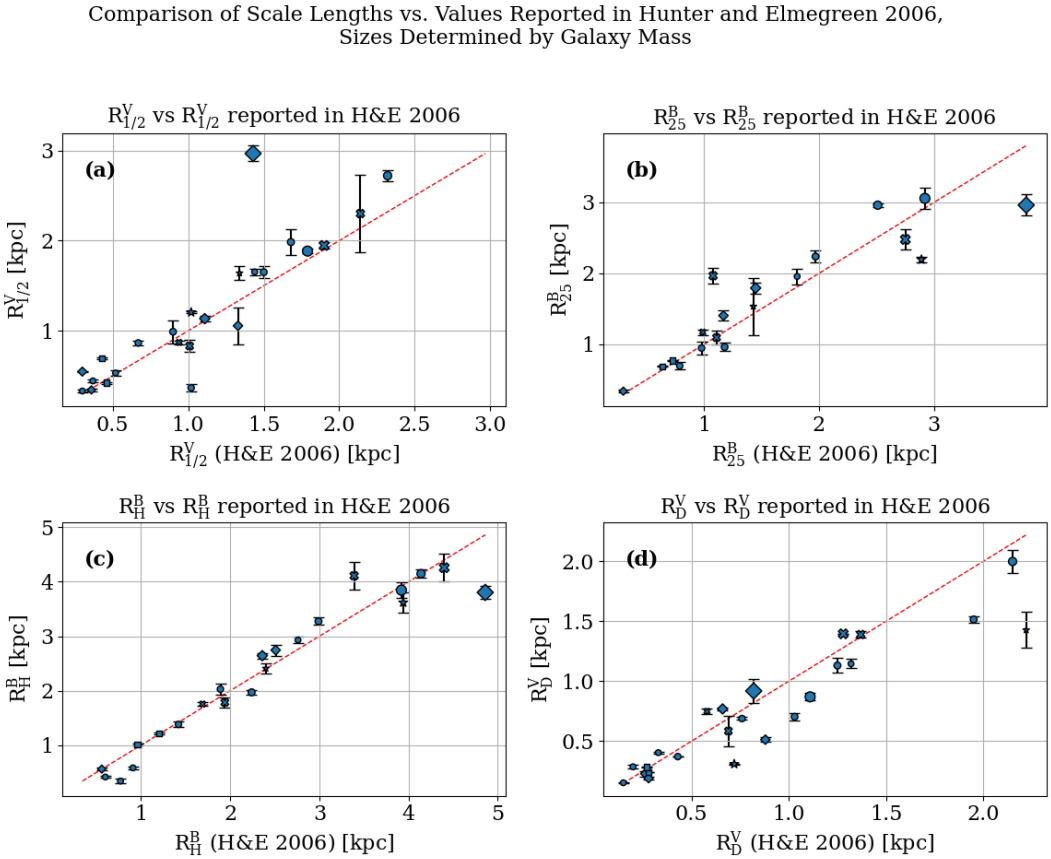


Figure 7: Comparison of scale lengths with Hunter & Elmegreen (2006) [2]: (a) $R^V_{1/2}$, (b) $R^B_{25}$, (c) $R^B_H$, (d) $R^V_D$, each against the published values. The size of each symbol is dictated by its $\log_{10}$(Galaxy mass).

to better reflect the ionizing photon production, extinction characteristics, and low-mass stellar populations of dwarf irregular galaxies. This calibration assumes a Salpeter IMF appropriate for dwarfs, where the lower bound for stellar mass is 0.1 $M_\odot$ and the upper bound is set to 100 $M_\odot$ [2]. Subsequent studies, including Murphy et al. (2011) [21] and Hao et al (2011) [22], have updated the calibration using modern stellar population synthesis models and a Kroupa IMF [24], which produce similar constants ($\sim$5–6 $\times 10^{-42}$ $M_\odot$ yr$^{-1}$ per erg s$^{-1}$). Since Equation 15 has been optimized specifically for dwarf irregular galaxies, and to maintain consistency, we adopted this calibration throughout our analysis.

We compared our recent star formation rate (SFR) measurements with those reported by Hunter and Elmegreen (2004) [2]. Figure 8 shows this comparison, where our $\log_{10}$SFR values from Table 2 are plotted against the literature. Symbol sizes scale with galaxy mass, colors indicate the instrument used to obtain the $H_\alpha$ image, and shapes distinguish galaxy types. Our results demonstrate strong consistency with the values reported in their study (Pearson $r = 0.98$).

We further compared our SFR measurements with those of Karachentsev and Kaisina (2013) [25], who also studied star formation in nearby dwarf irregulars. Eighteen galaxies

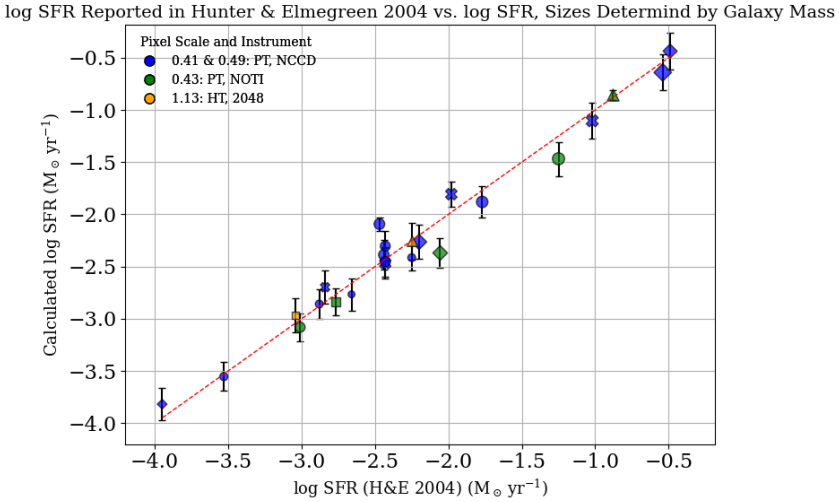


Figure 8: Comparison of our $\log_{10}$ SFR values with those reported by Hunter and Elmegreen (2004). Symbol sizes scale with $\log_{10}$(Galaxy mass), colors denote instrument, and shapes represent galaxy type.

are common to both samples. Unlike the Hunter & Elmegreen comparison, the $H_\alpha$ imaging in their work originates from independent databases and telescopes, making this comparison particularly significant. All the observations were carried out at the Special Astrophysical Observatory of the Russian Academy of Sciences (SAO RAS) with the Bol'shoi Teleskop Azimutal'nyi (BTA) 6-m telescope equipped with the SCORPIO focal reducer [26]; a $2048 \times 2048$ CCD provides a $\sim 6.1'$ field of view with a scale of $0.18''$ pixel$^{-1}$ and an average seeing of $\sim 1.8''$. The images in $H_\alpha$+[N II] were obtained through a narrow-band interference filter $H_\alpha$ ($\lambda_{\rm eff} = 6555$ , $\Delta\lambda = 75$ ), and the stellar continuum was removed using two medium-band filters bracketing $H_\alpha$ (SED607: $\lambda = 6063$ , $\Delta\lambda = 167$ ; SED707: $\lambda = 7063$ , $\Delta\lambda = 207$ ) [27]. Typical exposure times were $2 \times 600$ s in $H_\alpha$ and $2 \times 300$ s in the continuum. It is important to note that Karachentsev and Kaisina report SFRs using the Kennicutt calibration (Equation 14), whereas we adopt the dwarf-optimized Equation 15; nonetheless, the resulting SFRs are in excellent agreement (Pearson $r = 0.96$). Figure 9 presents this comparison, with symbol sizes scaling with galaxy mass and shapes indicating galaxy type. The strong consistency across independent datasets attests to the robustness of our SFR determinations.

# 6 Summary

In this study, we used data from optical and $H_\alpha$ wavelengths to better understand the star formation process in local Dwarf Irreguar galaxies. We find that scale lengths derived from $V$-band images, including the half-light radius and exponential disk scale length, show strong correlations not only with each other but also with scale lengths calculated from $B$-band data, such as $R_B^{25}$ and the Holmberg radius (Fig. 7). We also compare recent star formation rates, traced by $H_\alpha$ emission, with optical properties such as the half-light radius and $V$-band magnitude.

Our results are compared with Hunter & Elmegreen (2004, 2006) [2,3], with whom we

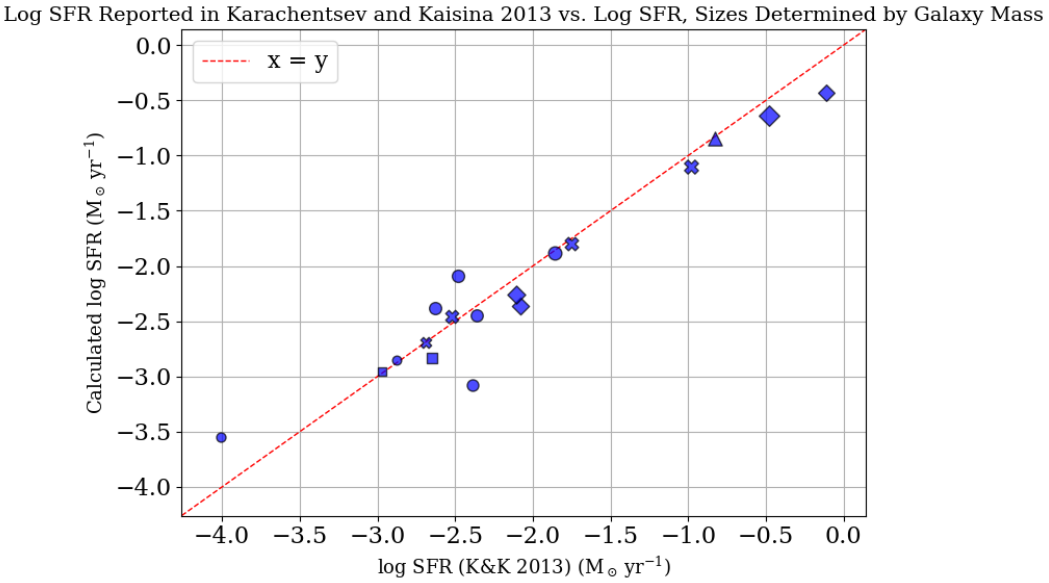


Figure 9: Comparison of our log(SFR) values with those reported by Karachentsev and Kaisina [25]. Symbol sizes scale with $\log_{10}$(Galaxy mass) and Symbols denote galaxy type. For a description of symbols, please refer to 5

share the LITTLE THINGS dataset, as well as with Karachentsev & Kaisin (2013) [25], who employed independent $H_\alpha$ data [27]. Our analysis reveals a strong correlation between recent SFR and $V$-band properties, suggesting a link between gas dynamics and stellar scale lengths. This correlation implies that recent star formation over the past few million years is connected to older star formation activity ($\sim$ 1 Gyr), hinting that the formation of older stars may influence or trigger new star formation in dwarf irregular galaxies.

## Authors' Contributions

All authors have the same contribution.

## Data Availability

All FITS files used in this study are publicly available on the National Radio Astronomy Observatory (NRAO) website.

## Conflicts of Interest

The authors declare that there is no conflict of interest.

## Ethical Considerations

The authors have diligently addressed ethical concerns, such as informed consent, plagiarism, data fabrication, misconduct, falsification, double publication, redundancy, submission, and other related matters.

## Funding

This research did not receive any grant from funding agencies in the public, commercial, or nonprofit sectors.

## Appendix A: Observational Details

Table 3: Observational details for all the objects utilized for this paper.

| Object | Type | Filter | Exposure (s) | Instrument | Pixel Scale (″) |
|---|---|---|---|---|---|
| DDO 43 | Im | B | 1800 | LO1.1m | 1.13 |
| | | V | 900 | LO1.1m | 1.13 |
| | | $H_\alpha$ | 3000 | PT, FP, NCCD | 0.49 |
| | | $H_\alpha$ (cont. sub) | 3000 | PT, FP, NCCD | 0.49 |
| DDO 46 | Im | B | 1800 | LO1.1m | 1.13 |
| | | V | 1200 | LO1.1m | 1.13 |
| | | $H_\alpha$ | 3000 | PT, FP, NCCD | 0.49 |
| | | $H_\alpha$ (cont. sub) | 3000 | PT, FP, NCCD | 0.49 |
| DDO 47 | IB(s)m | B | 1800 | LO1.1m | 1.13 |
| | | V | 1200 | LO1.1m | 1.13 |
| | | $H_\alpha$ | 3000 | PT, FP, NCCD | 0.49 |
| | | $H_\alpha$ (cont. sub) | 3000 | PT, FP, NCCD | 0.49 |
| DDO 50 | Im | B | 2400 | LO1.1m | 1.13 |
| | | V | 1200 | LO1.1m | 1.13 |
| | | $H_\alpha$ | 1800 | PT, 4:1, NOTI | 0.43 |
| | | $H_\alpha$ (cont. sub) | 1800 | PT, 4:1, NOTI | 0.43 |
| DDO 52 | Im | B | 1800 | LO1.1m | 1.13 |
| | | V | 900 | LO1.1m | 1.13 |
| | | $H_\alpha$ | 2700 | PT, 4:1, NOTI | 0.43 |
| | | $H_\alpha$ (cont. sub) | 2700 | PT, 4:1, NOTI | 0.43 |
| DDO 63 | IAB(s)m | B | 1900 | LO1.1m | 1.13 |
| | | V | 1200 | LO1.1m | 1.13 |
| | | $H_\alpha$ | 1800 | HT, 2048 | 1.13 |
| | | $H_\alpha$ (cont. sub) | 1800 | HT, 2048 | 1.13 |
| DDO 69 | Ibm | B | 2400 | LO1.1m | 1.13 |
| | | V | 1200 | LO1.1m | 1.13 |
| | | $H_\alpha$ | 3000 | PT, FP, NCCD | 0.49 |
| | | $H_\alpha$ (cont. sub) | 3000 | PT, FP, NCCD | 0.49 |
| DDO 87 | Im | B | 2400 | LO1.1m | 1.13 |
| | | V | 1200 | LO1.1m | 1.13 |
| | | $H_\alpha$ | 3000 | PT, FP, NCCD | 0.49 |
| | | $H_\alpha$ (cont. sub) | 3000 | PT, FP, NCCD | 0.49 |
| DDO 101 | Im | B | 1800 | LO1.1m | 1.13 |
| | | V | 1200 | LO1.1m | 1.13 |
| | | $H_\alpha$ | 2400 | PT, FP, NCCD | 0.49 |

Continued on next page

Table 3 – Continued from previous page

| Object | Type | Filter | Exposure (s) | Instrument | Pixel Scale (″) |
|---|---|---|---|---|---|
| | | $H_\alpha$ (cont. sub) | 2400 | PT, FP, NCCD | 0.49 |
| DDO 126 | IBm | B | 1800 | LO1.1m | 1.13 |
| | | V | 1200 | LO1.1m | 1.13 |
| | | $H_\alpha$ | 1800 | PT, 4:1, NOTI | 0.43 |
| | | $H_\alpha$ (cont. sub) | 1800 | PT, 4:1, NOTI | 0.43 |
| DDO 133 | Im | B | 1800 | LO1.1m | 1.13 |
| | | V | 1200 | LO1.1m | 1.13 |
| | | $H_\alpha$ | 2700 | PT, FP, NCCD | 0.49 |
| | | $H_\alpha$ (cont. sub) | 2700 | PT, FP, NCCD | 0.49 |
| DDO 154 | Ibsm | B | 1200 | LO1.1m | 1.13 |
| | | V | 600 | LO1.1m | 1.13 |
| | | $H_\alpha$ | 2700 | PT, 4:1, NCCD | 0.41 |
| | | $H_\alpha$ (cont. sub) | 2700 | PT, 4:1, NCCD | 0.41 |
| DDO 155 | Im | B | 1800 | LO1.1m | 1.13 |
| | | V | 1200 | LO1.1m | 1.13 |
| | | $H_\alpha$ | 1800 | PT, 4:1, NCCD | 0.41 |
| | | $H_\alpha$ (cont. sub) | 1800 | PT, 4:1, NCCD | 0.41 |
| DDO 165 | Im | B | 1800 | LO1.1m | 1.13 |
| | | V | 1200 | LO1.1m | 1.13 |
| | | $H_\alpha$ | 2300 | PT, FP, NCCD | 0.49 |
| | | $H_\alpha$ (cont. sub) | 2300 | PT, FP, NCCD | 0.49 |
| DDO 167 | Im | B | 1200 | LO1.1m | 1.13 |
| | | V | 900 | LO1.1m | 1.13 |
| | | $H_\alpha$ | 3000 | PT, FP, NCCD | 0.49 |
| | | $H_\alpha$ (cont. sub) | 3000 | PT, FP, NCCD | 0.49 |
| DDO 168 | IBm | B | 1800 | LO1.1m | 1.13 |
| | | V | 1200 | LO1.1m | 1.13 |
| | | $H_\alpha$ | 2400 | PT, FP, NCCD | 0.49 |
| | | $H_\alpha$ (cont. sub) | 2400 | PT, FP, NCCD | 0.49 |
| DDO 187 | Im | B | 1800 | LO1.1m | 1.13 |
| | | V | 1200 | LO1.1m | 1.13 |
| | | $H_\alpha$ | 3000 | PT, FP, NCCD | 0.49 |
| | | $H_\alpha$ (cont. sub) | 3000 | PT, FP, NCCD | 0.49 |
| NGC 1156 | IBm | B | 1800 | LO1.1m | 1.13 |
| | | V | 1200 | LO1.1m | 1.13 |
| | | $H_\alpha$ | 3000 | PT, FP, NCCD | 0.49 |
| | | $H_\alpha$ (cont. sub) | 3000 | PT, FP, NCCD | 0.49 |
| NGC 1569 | IBm | B | 180 | KPNO4m | 0.42 |
| | | V | 60 | KPNO4m | 0.42 |
| | | $H_\alpha$ | 3000 | PT, FP, NCCD | 0.49 |
| | | $H_\alpha$ (cont. sub) | 3000 | PT, FP, NCCD | 0.49 |
| NGC 2366 | IB(s)m | B | 480 | KPNO4m | 0.42 |
| | | V | 180 | KPNO4m | 0.42 |
| | | $H_\alpha$ | 1800 | PT, FP, NCCD | 0.49 |
| | | $H_\alpha$ (cont. sub) | 1800 | PT, FP, NCCD | 0.49 |
| NGC 4163 | IAm | B | 1800 | LO1.1m | 1.13 |
| | | V | 1800 | LO1.1m | 1.13 |
| | | $H_\alpha$ | 1800 | HT, 2048 | 1.13 |
| | | $H_\alpha$ (cont. sub) | 1800 | HT, 2048 | 1.13 |

Continued on next page

Table 3 – Continued from previous page

| Object | Type | Filter | Exposure (s) | Instrument | Pixel Scale (″) |
|---|---|---|---|---|---|
| NGC 4214 | IAB(s)m | B | 480 | KPNO4m | 0.42 |
| | | V | 180 | KPNO4m | 0.42 |
| | | $H_\alpha$ | 900 | PT, 4:1, NOTI | 0.43 |
| | | $H_\alpha$ (cont. sub) | 900 | PT, 4:1, NOTI | 0.43 |
| UGC 8508 | IAm | B | 1800 | LO1.1m | 1.13 |
| | | V | 1200 | LO1.1m | 1.13 |
| | | $H_\alpha$ | 1800 | PT, 4:1, NOTI | 0.43 |
| | | $H_\alpha$ (cont. sub) | 1800 | PT, 4:1, NOTI | 0.43 |
| WLM | IB(s)m | B | 2400 | LO1.1m | 1.13 |
| | | V | 1200 | LO1.1m | 1.13 |
| | | $H_\alpha$ | 3000 | PT, FP, NCCD | 0.49 |
| | | $H_\alpha$ (cont. sub) | 3000 | PT, FP, NCCD | 0.49 |

Values reported from Hunter and Elmegreen (2006) [3] and Hunter and Elmegreen (2004) [2] for optical and $H_\alpha$ data, respectively.

# References


[1] Hunter, D. A., Ficut-Vicas, D., Ashley, T., et al. 2012, AJ, 144, 134.

[2] Hunter, D. A., & Elmegreen, B. G. 2004, AJ, 128, 2170.

[3] Hunter, D. A., & Elmegreen, B. G. 2006, ApJS, 162, 49.

[4] Leroy, A. K., Bigiel, F., de Blok, W. J. G., Bolatto, A. D., Brinks, E., Madore, B., & Murphy, E. 2012, AJ, 144, 3.

[5] de Vaucouleurs, G. 1959, in Handbuch der Physik, 53, 275.

[6] de Vaucouleurs, G., de Vaucouleurs, A., Corwin, H. G., Buta, R. J., Paturel, G., & Fouqué, P. 1991, Third Reference Catalogue of Bright Galaxies (New York: Springer) (RC3).

[7] Holmberg, E. 1958, Meddelanden från Lunds Astronomiska Observatorium, Ser. II, 136, 1.

[8] de Vaucouleurs, G., de Vaucouleurs, A., & Corwin, H. G. 1976, Second Reference Catalogue of Bright Galaxies (Austin: Univ. Texas Press) (RC2).

[9] Freeman, K. C. 1970, ApJ, 160, 811.

[10] de Jong, R. S. 1996, A&AS, 118, 557.

[11] Caldwell, N., & Bothun, G. D. 1987, AJ, 94, 1126.

[12] Impey, C., Bothun, G., & Malin, D. 1988, ApJ, 330, 634.

[13] Kennicutt, R. C., Jr. 1998, ARA&A, 36, 189.

[14] Rosenfeld, A., & Kak, A. C. 1976, Digital Picture Processing (New York: Academic Press).

[15] Lee, J. S. 1980, IEEE Trans. Pattern Anal. Mach. Intell., 2, 165.

[16] Sharma, A., Bhateja, V., & Tripathi, A. 2016, in Information Systems Design and Intelligent Applications, ed. S. C. Satapathy et al., Advances in Intelligent Systems and Computing, Vol. 434 (New Delhi: Springer), 663.

[17] Buades, A., Coll, B., & Morel, J.-M. 2005, in Proc. IEEE Comput. Soc. Conf. Comput. Vis. Pattern Recognit. (CVPR), 2, 60.

[18] Efron, B. 1979, Ann. Statist., 7, 1.

[19] Cardelli, J. A., Clayton, G. C., & Mathis, J. S. 1989, ApJ, 345, 245.

[20] Kennicutt, R. C., Jr. 1998, ARA&A, 36, 189.

[21] Murphy, E. J., Condon, J. J., Schinnerer, E., Kennicutt, R. C., Calzetti, D., Armus, L., et al. 2011, ApJ, 737, 67.

[22] Hao, C.-N., Kennicutt, R. C., Jr., Johnson, B. D., Dale, D. A., Calzetti, D., Moustakas, J., et al. 2011, ApJ, 741, 124.

[23] Salpeter, E. E. 1955, ApJ, 121, 161.

[24] Kroupa, P. 2001, MNRAS, 322, 231.

[25] Karachentsev, I. D., Kaisin, S. S . 2013, AJ, 146, 46.

[26] Afanasiev, V. L., & Moiseev, A. V., 2005, Astronomy Letters, 31, 194.

[27] Karachentsev, I. D., Kaisin, S. S., 2010, AJ, 140, 1241.